RSC Advances

ROYAL SOCIETY OF CHEMISTRY

www.rsc.org/advances

Cite this: DOI: 10.1039/c0xx00000x

www.rsc.org/xxxxxx

ARTICLE TYPE

3D-hierarchical SnS nanostructures: controlled synthesis, formation mechanism and lithium-ion storage performances

Shuankui Li[a,b], Jiaxin Zheng[a], Zongxiang Hu[a], Shiyong Zuo[b], Zhiguo Wu[b,], Pengxun Yan[b], and Feng Pan[a,*]*

Received (in XXX, XXX) Xth XXXXXXXXX 20XX, Accepted Xth XXXXXXXXX 20XX
DOI: 10.1039/b00000

A series of SnS nanocrystals with tunable morphology and sheet thickness have been prepared through a solvothermal method and by introducing selective additives to the solution. Such SnS nanocrystals exhibit hierarchical hollow structures of SnS nanoflowers assembled from nanosheets. The formation of the SnS hollow micro-flowers is based on an inside-out Ostwald ripening mechanism. By adjusting the additive and concentration, we can grow SnS nanosheet with about 14nm thick, in which thickness the band gap of SnS can be expected to increase so as to give an opportunity to explore the structure-related novel properties and superior device performances. As one application for these SnS nanostructure, properties vs. morphology for lithium storage were investigated, and it is shown that the SnS porous sphere built with scale-like ultrathin nanosheets exhibited the best performance.

Introduction

Hierarchical micro/nanostructures, which are based upon zero-dimensional (0D), one-dimensional (1D), and two-dimensional (2D) micro/nanoscale building blocks, have attracted much attention due to their importance of fundamental research, such as dimensionality and quantum size effects.[1-3] Therefore, the synthesis of these advanced functional nanostructures with full controlled size and morphology is very important in nanoscience.[4-5] For the syntheses of nano-materials with precisely controlled sizes and morphologies, the solution-based approach is quite effective, because it could be mostly achieved by controlling the reaction kinetics and tuning the interface ligand chemistry. However, the crystallization and anisotropic growth of nanomaterials in the solution is usually complex, which is still not fully understood. Even though many advances in fabricating nanomaterials have been achieved, how to control the morphologies of nano-crystals and the related mechanisms are still interesting and need to be further explored.

Recently, narrow band gap IV–VI compound semiconductors such as SnS, SnSe, GeS, and PbS, have attracted great attention due to their desirable and tunable optoelectronic properties. In particular, tin(II) sulfide (SnS) has gained increasing attention because of its natural abundance and widely applied in many fields such as solar cells, field effect transistors, photodetectors, and electrochemical capacitors, photocatalysis, as well as Li ion battery anodes .[6-8] Bulk SnS is a p-type semiconductor with an indirect band gap of 1.07eV and a direct band gap of 1.3eV that exhibits a high absorption coefficient and high hole mobility. Additionally, the exciton Bohr radius of SnS is estimated to be ~7nm, thus the band gap of SnS can increase for particles with diameters on the order of 14nm or less due to quantum confinement effects, which means that the size and morphology of nanocrystals is crucial to the optoelectronic properties.[9] Moreover, with a strongly distorted NaCl structure (orthorhombic: Pnma), SnS consists of two-atom-thick Sn-S layers extend in the b and c-directions, while the interlayer bonding, extending in the a-direction to connect the Sn-S slabs, is a weak van der Waals interaction.[9] These bonding characteristics, therefore, impart the anisotropy of the structure of GeS-type SnS by providing a chemical driving force for SnS crystallites to adopt two-dimensional (2D) morphologies, including nanosheets,[10] nanoplates,[11] and nanobelts.[12]

Rational design and manipulation of nanostructures, including the phase, size, and morphology, play crucial roles in the property enhancement.[13-20] Therefore, enormous efforts have been devoted to phase and morphology controlled synthesis to explore novel properties and superior device performances.[21] Wang et al. obtained 2D SnS nanosheets in solution phase.[10] Kim et al. grow two-dimensional (2D) SnS nanosheets electrode on metallic current collectors with a chemical vapor deposition (CVD) method.[11] Schaak et al. synthesized the SnS nanoflowers in solution phase.[22] However, no work reports on how to control the morphology and thickness of the 2D layered structure. Compared with the reported two-dimensional nanostructures, the SnS hierarchical structures produced by self-assembly and higher order organization of nanosheet building blocks would show special properties, since the novel spatial arrangement can provide both extraordinarily high activated surface area and anisotropic robustness. Therefore, synthesis of 3D hierarchical structures with tunable morphology, and especially with tunable thickness for the nanosheet crystals would be an interesting and challenging work for SnS.

In the present work, we demonstrate the controllable growth of a series of 3D-hierarchical SnS nanostructures with tunable morphology by the citric acid or salt assisted ethylene glycol (EG) solvent. An Ostwald ripening mechanism is proposed to explain the formation of such 3D-hierarchical SnS hollow nanostructures. Interestingly, by adjusting the additive and concentration, we can grow 3D-hierarchical SnS nanostructures with the tunable morphology and the sheet thickness, which give an opportunity to explore the structure-related novel properties and superior device performances. As one application for these SnS nanostructure, properties vs. morphology for lithium storage were investigated. It is shown that the SnS porous sphere built with scale-like ultrathin nanosheets exhibited the best performance, because of the short diffusion length for lithium ions determined by the small thickness of nanosheets, better interconnection between building blocks, and high porosity for efficient transport of lithium ions.

Experiment

Materials and preparation

All the reagents were analytical grate and used without further purification. In a typical synthesis, 226mg $SnCl_2$•$2H_2O$ (1mmol), 228mg CH_4N_2S (3mmol) and 226mg (1mmol) citric acid were dissolved into 30ml ethylene glycol (EG) under vigorous magnetic stirring to form an even solution. Then the resulting solution was transferred into a Teflon-lined stainless autoclave (40ml capacity), followed by hydrothermal treatment at 180 °C for 18h. After the treatment, the black products were collected by filtration, successively washed several times with deionized water and absolute ethanol, and dried at 60 °C for 24h.

Electrochemical measurements

CR2016 type half cells were assembled with the prepared samples as the anode material in a high-purity argon-filled glove box. The anodes were prepared by mixing active materials, carbon black, and polyvinylidene difluoride (PVDF) at a weight ratio of 70:20:10 in NMP (N-methyl-2-pyrrolidone) solvent to form slurry. The typical loading density on a Cu foil was ~2mg/cm^2. A Li foil was used as the cathode. $LiPF_6$ (1M) in ethylene carbonate (EC)/diethyl carbonate (DEC) (1:1 w/w) was used as the electrolyte. Cyclic voltammetry was carried out between 1.5V and 0.02V at a scan rate of 0.1mV/s using an electrochemical workstation (CHI 660E). The charge/discharge tests were performed in a voltage window of 0.02-1.5V at different current densities using a multi-channel battery workstation (lande Co., China).

Characterization

The crystal structures, morphologies, microstructures, and compositions of the as-synthesized products were characterized by X-ray diffraction (XRD) on a Philips X'Pert Pro Diffractometer, using Cuα1 radiation (λ=1.54056Å), field-emission scanning electron microscopy (SEM, HitachiS-4800), transmission electron microscopy (TEM, JEOL-2010).

Results and Discussion

Fig.1a shows the power X-ray diffraction (XRD) pattern of the SnS hollow micro-flowers. All of the diffraction peaks can be indexed as α-SnS, which is in good agreement with the value reported in the literature (JCPDS Card No.39-0354). No diffraction peaks from any other impurities were observed, indicating the high purity of the products. The intensity of the peak at 2θ=32.1° indexed as (400) is significantly enhanced compared with that for the standard sample, showing that the SnS product mostly has exposed facets of the {100} family. Compared with those of the bulk material, the peaks were relatively broadened, which demonstrated that the SnS have a small crystal size.

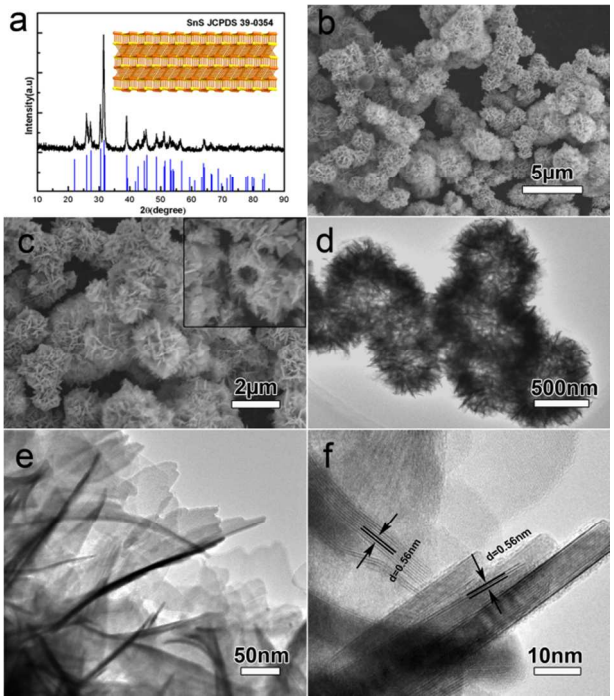

Fig.1. (a) A typical XRD pattern of the as-prepared SnS hollow micro-flowers. The inset shows its corresponding crystalline structure. The low (b) and high (c) magnification FE-SEM images of the as-prepared SnS hollow micro-flowers. (d) TEM and (e, f) HRTEM images of the as-prepared SnS hollow micro-flowers.Scanning electron microscopy (SEM) reveals that the sample consists of discrete and uniform flower-like microspheres (Fig.1b and c). In particular, some open pores with 100nm in wall thickness in Fig.1c obviously indicate the hollow structure of the sample (inset in Fig.1c), which can also be verified by the TEM observation. The TEM images further show the hierarchical structure loosely assembled from large continuous nanosheets with relatively small thickness of about 10-20nm (Fig.1d). More interestingly, the micro-flowers exhibit a hollow interior of about 200nm as evidenced by the distinct brightness contrast in the central region. The HRTEM image (Fig.1e) displays that the thicknesses of these nanosheets is about 20nm. The HRTEM images of both top view and side view of a SnS nanosheet (Fig.1f) show that it is single crystalline with the normal of the primary surfaces along a-direction, which means that the SnS product mostly has exposed facets of the {100} family. Thus, a unique hierarchical hollow sphere assembled from SnS nanosheets was discerned, and the large extra spaces may enhance the structural integrity by holding volume changes during continual discharge/charge cycles. Also, the ultrathin two-dimensional (2D) structures can shorten the lithium ion diffusion length. These above favorable points guarantee this SnS hollow micro-flower with outstanding electrochemical performances.

To reveal the growth process of SnS hollow micro-flowers and possible growth mechanism, the study of the morphology evolution of samples with different reaction times had been

conducted, as shown in Fig.2. When the hydrothermal time was 2h, it can be seen that the product was entirely comprised of solid nanospheres. There are some sheets-like units appeared on its surface (Fig. 2a). As the hydrothermal process was prolonged to 4h, nanosheets further grew (Fig. 2b). As the reaction proceeds, the larger crystallites located on the surfaces serve as crystal seeds for the subsequent crystallization process and crystal growth. As a result, the outer crystallites become larger by merging with the smaller crystallites from inside, which results in the formation of hollow cores, as shown in Fig. 2c. Finally, after prolonging the reaction time further to 18h, the whole process is complete (Fig. 2d and g). The corresponding XRD patterns of the samples obtained at different reaction times (Fig.3) display the gradual increase of the crystallinity of the samples, which is agree with the inside-out Ostwald ripening mechanism.

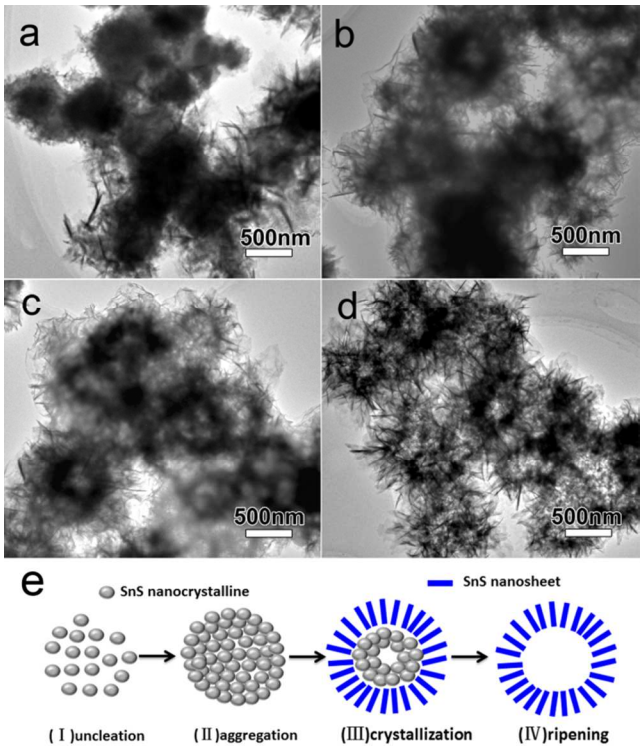

Fig.2. TEM images showing the evolution process of SnS hollow micro-flowers for different reaction periods: (a) 2h, (b) 4h, (c) 12h, and (d) 18h. (e) The formation process of the SnS hollow micro-flowers.

On the basis of the above morphology and crystallinity evolution in the time-dependent experiments, it is believed that Ostwald-ripening process should be the main driving force for the formation of the SnS hollow micro-flowers. As illustrated in Fig. 2e, SnS tiny nanoparticles were formed at the early stage, followed by self-aggregated to form amorphous solid spheres in order to minimize the total surface energy. As the reaction proceeds, the larger crystallites located on the surfaces serve as crystal seeds for the subsequent crystallization process and crystal growth. The larger particles grew at the cost of the smaller ones due to the different solubility between relatively larger and smaller particles. Following the general expression of Gibbs law, the driving force for crystal growth is to minimize the total surface free energy of the system. Subsequently, SnS crystal growth according to its growing habit should further reduce the interface energy between primary nanoparticles. In the case of the orthorhombic structure of SnS, the (100) facets are the most stable facets due to the strongest ionic interactions.[9] It is rational that the SnS nanostructure tends to expose (100) facets, which is also proved in the section of " investigation of growth mechanism by first principles calculations" . In the subsequent steps, the metastable SnS smaller crystallites inside of sphere are dissolved and then adsorbed selectively onto the thermodynamically unfavoured (010) and (002) facets of orthorhombic SnS, leaving the formation of SnS nanosheets on the surface of the sphere. Finally, the SnS hollow micro-flowers assembled from nanosheets are formed. A similar ripening mechanism has also been proposed by many groups for hydrothermal preparation of various inorganic hollow nanospheres. [23- 25]

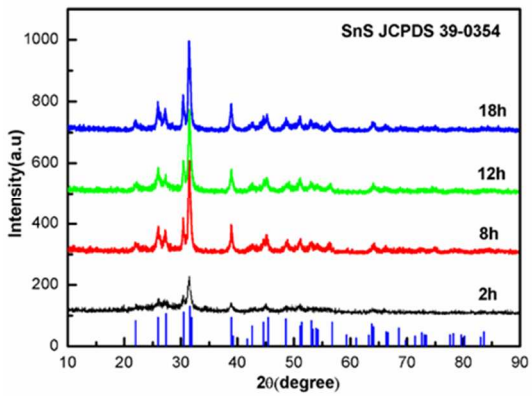

Fig.3. XRD patterns of as-prepared samples for different reaction periods.

In our experiment, the citric acid plays an important role in controlling the final morphology of products. Compared with the as-prepared sample synthesized with the citric acid concentration of 1mmol (Fig. 4e-f), the SnS nanosheets grown with the citric acid concentration of 0.5 mmol are thicker (Fig. 4c-d). This tendency is further observed in the sample synthesized without adding citric acid (Fig. 4a-b). All of the above results indicate that the concentration of citric acid has a large effect on the thickness of the SnS nanosheet. In the controlled experiments, sodium citrate was also used instead of citric acid under the same conditions. When the 0.5mmol sodium citrate was introduced to the solution, novel porous micro-spheres with coarse surfaces and big size of about 10μm formed (Fig. 4g-h). Interestingly, the micro-spheres were constructed by many scale-like ultrathin nanosheets with the average thickness of 16 nm, which were densely packed and formed a multi-layered structure. Once the amount of sodium citrate was increased to 1mmol, the porous micro-spheres constructed from porous ultrathin nanosheet could be observed (Fig. 4i-j).

Based on the above results, it is found that the thickness of the SnS nanosheet building units show obvious difference with different prepared conditions. Interestingly, it is reveals that the sample synthesized without adding citric acid has thicker building units with an average thickness of 89nm. As the amount of citric acid increased, the average thickness slightly reduced to 56.6nm and finally to 32nm (1mmol citric acid). However, when the sodium citrate introducing to the solution, the average thickness decreased rapidly to 16nm, and finally to porous nanosheet (1mmol sodium citrate). The all above results suggest that either additives or concentration is crucial for tunable thickness of the nanosheets for the synthesis of ordered SnS hierarchical structures.

According to literatures, for SnS crystals, the (100) surface is the most stable, which will lead to the anisotropy growth for SnS, and the final SnS crystals would mostly exposed (100) facets

consistent with the experimental observations. Most (100)-oriented SnS sheets or plates are prepared under solvothermal conditions, typically using ethylene glycol as the solvent. If we introduce additives with stronger absorption on the (100) surface to the solvent during the synthesis process, the more stable (100) surface will be formed and thinner SnS sheets or plates can be obtained. Therefore, citric acid is an appropriate additive to tune the thickness of the SnS sheets during the synthesis process. For the case of sodium citrate, the citrate may absorption on the (100) surface easier, thus leading to the thinner thickness of SnS nanosheet under the same concentration as citric acid.

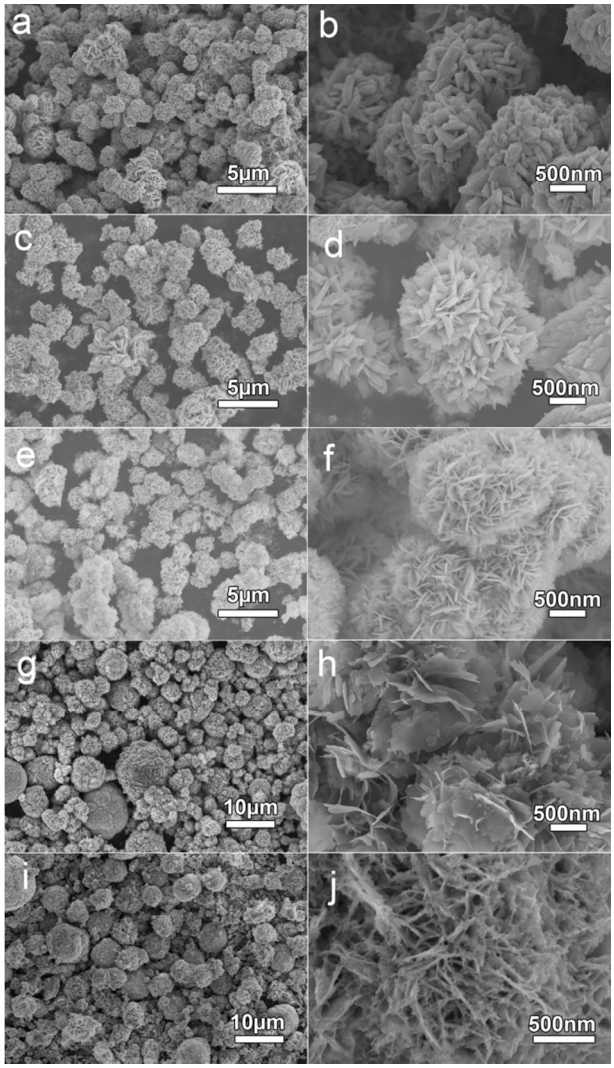

Fig.4. The SEM images of samples prepared prepared with different additives concentration. (a, b) 0 mmol citric acid (CA), (c, b) 1mmol citric acid, (e, f) 0.5mmol citric acid, (g, h) 0.5mmol sodium citrate (SC), (i, j) 1mmol sodium citrate.

SnS is considered as one of the promising anode materials for the next generation lithium-ion batteries, owing to its high theoretical specific lithium storage capacity of 792mAh/g.[26] According to previous reports, the lithium intercalation and conversion reactions of SnS based on the formation of metallic Sn and subsequent generation of a Li-Sn alloy: [26]

$$SnS + xLi^+ + xe^- \rightarrow Li_2S + Sn \quad (1)$$

$$Sn + xLi^+ + xe^- \leftrightarrow Li_xSn\ (0 \leqslant x \leqslant 4.4) \quad (2)$$

It is well known that the reversible lithium storage capability of SnS is essentially attributed to the formation of Li-Sn alloys (eq. 2).[27] However, the large volume changes (~300%) during lithium insertion and extraction from SnS leads to breakage of electrical contact between particles and results in quick capacity decline upon extended cycling. The unique structure of the 3D SnS hierarchical architectures could partly overcome such a problem in virtue of the high porosity and short diffusion length. Thus, a series of electrochemical measurements were performed on the SnS hierarchical architectures to study the lithium storage properties.

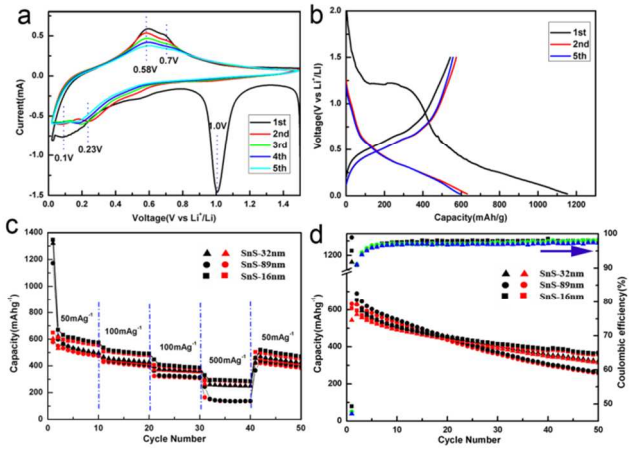

Fig. 5. (a) CV of SnS hollow micro-flowers in the first five cycles at the scan rate of 0.1mV/s. (b) Typical galvanostatic charge–discharge curves of SnS hollow micro-flowers at a current density of 100mA/g.(c) Cycling performance and (d) rate capability of sample SnS-32nm, SnS-89nm, and SnS-16nm.

In order to investigate the electrochemical details of the as-prepared 3D-hierarchical SnS nanostructures, cyclic voltammetric experiments were initially conducted between 0.02 and 1.5 V at a scan rate of 0.1mV/s (Fig.5a). The peaks above 1.0V in the first charge cyclic voltammetry curves correspond to the displacement reaction of Li and SnS which is shown in Eq. (1), and similar results have previously been reported for SnO_2 and SnS_2.[28, 29] The decomposition of the SnS into metallic Sn and Li_2S as well as the formation of solid electrolyte interface (SEI) may lead to the large irreversibility of SnS-based anodes at the first charge/discharge cycle.[30] Therefore, this surface structure may affect the formation of irreversible SEI layer on the anode surface, which results in a low coulombic efficiency of the first cycle. The more cathodic potential at around 0.1V and 0.23V and the anodic potential at about 0.5V in the first scan are known to represent the redox peak couple of reaction (2). [24] Such a redox peak couple was frequently observed in a similar potential range in the following cycles, indicating that Li ions subsequently reacted with Sn metal to form Li_xSn alloy as well as the reverse reaction. From the second cycle onwards, the CV curves mostly overlap, indicating the good reversibility of the electrochemical reactions. Fig.5b shows the charge-discharge voltage profile of SnS flowerlike hollow nanosphere measured at a current density of 100mA/g. In agreement with this CV result, two poorly defined plateaus can be identified in the first discharge process, and it gives a high discharge capacity of 1153 mAh/g. The following charge process features a charge capacity of 762mAh/g, which is 98% of the maximum theoretical reversible capacity of SnS. As

above mentioned, the formation of solid electrolyte interface (SEI) film and irreversible reaction in Eq (1) may be responsible for the low initial coulombic efficiency of sample. Moreover, the coulombic efficiency is increased up to 92.0% in the second cycle and keeps increasing in the following cycles.

Because of its high theoretical specific lithium storage capacity of 792mAh/g, SnS is considered as one of the promising anode materials for the next generation lithium-ion batteries.[11] Fig. 5c and d show the electrochemical performance. It is evident that the SnS nanoflowers assembled with 16nm thick nano-sheets (denoted as SnS-16nm) manifest a greatly enhanced lithium storage capability as compared to the two counterparts. After 50 discharge and charge cycles at a current density of 100mA/g, a higher reversible capacity of 410mAh/g was delivered by SnS-16nm, while the two counterparts only give 370mAh/g and 306mAh/g, respectively. Moreover, the rate performance of SnS-16nm was also noticeably higher than that of SnS-32nm and SnS-89nm, which agrees with the cycle performance. SnS-16nm delivered a specific capacity of 669mAh/g at a current density of 50mA/g, 537mAh/g at a current density of 100mA/g, 450mAh/g at a current density of 200 mA/g, and 330mAh/g at a current density of 500mA/g, respectively. At the end of 50 cycles, a capacity of 520mAh/g at a current density of 50mA/g was retained even after several cycles at various current densities (Fig.5c). The improved cycling stability and rate capability of SnS-16nm might be attributed to the unique hierarchical SnS nanostructure built with ultrathin nanosheets. The ultrathin nanosheets could provide a short lithium ion diffusion path, compared with the thick nanosheet, such as SnS-32nm and SnS-86nm. Moreover, the thin thickness of the nanosheets might be favorable for the performance of the active material and increase the specific capacity, and accelerate the surface electrochemical reactions to increase the capacity and rate performance during the discharge-charge process.[31-33] The 3D-hierarchical structure constructed by tiny ultrathin nanosheets could relieve the structural alterations caused by the charge-discharge process; [32-34] offer a lager contact area between the electrode and electrolyte, which have been confirmed by the fact the performance of SnS-16nm better than the other samples built with thick nanosheets.

Conclusions

In summary, SnS hollow micro-flowers assembled from nanosheets have been successfully prepared by a citric acid assisted solvothermal method for the first time. It was found that the formation of the SnS hollow micro-flowers based on an inside-out Ostwald ripening mechanism. By introducing additives to the solution, a series of SnS 3D-hierarchical nanostructures with different morphology and the sheet thickness was synthesized. These 3D hierarchical structures provide several advantages for lithium storage, including a short diffusion length for lithium ions determined by the small thickness of nanosheets, better interconnection between building blocks, and high porosity for efficient transport of lithium ions.

Acknowledgements

This work is supported by Guangdong Innovation Team Project (No. 2013N080), Shenzhen Science and Technology Research Grant (No. ZDSY20130331145131323, CXZZ20120829172325895, JCYJ20120614150338154), and the National Natural Science Foundation of China (No. 11204114).

Notes and references

[a] *School of Advanced Materials, Peking University Shenzhen Graduate School, Shenzhen, 518055, China. E-mail: panfeng@pkusz.edu.cn.(Feng Pan)*

[b] *School of Physical Science and Technology, Lanzhou University, Lanzhou, Gansu, 730000, China. E-mail:zgwu@lzu.edu.cn.(Zhiguo Wu)*

1. A. Chakrabarti, J. Lu, A.M. McNamara, L.M. Kuta, S.M. Stanley, Z.L. Xiao, J.A. Maguire, N.S. Hosmane, Inorganica Chimica Acta, 2011, **374**, 627–631.
2. H.B. Wu, A.Q. Pan, H.H. Hang, X.W. Lou, *Adv. Funct. Mater.*, 2013, **23**, 5669-5674.
3. Y.Z. Zhang, H. Pang, Y.Q. Sun, W.Y. Lai, A. Wei, W.Huang, *Int. J. Electrochem. Sci.*, 2013, **8**, 3371 – 3378.
4. S.K. Li, S.Y.Zuo, Z.G. Wu, Y. Liu, R.F. Zhuo, J.J. Feng, D. Yan, J. Wang, P.X. Yan, Electrochimica Acta, 2015, **1**, 355–362.
5. H.X. Zhong, G.Z. Yang, H.W. Song, Q.Y. Liao, H. Cui, P.K. Shen, C.X. Wang, J. Phys. Chem. C, 2012, **116 (16)**, 9319-9326.
6. S.G. Hickey, C. Waurisch, B. Rellinghaus, A. Eychmuller, J. Am. Chem. Soc., 2008, **130**, 14978−14980.
7. A. de Kergommeaux, J. Faure-Vincent, A. Pron, R. de Bettignies, B. Malaman, P. Reiss, J. Am.Chem. Soc., 2012, **134**, 11659−11666.
8. X. Liu, Y. Li, B. Zhou, X.L. Wang, A.N. Cartwright, M.T. Swihart, Chem. Mater., 2014, **26**, 3515−3521.
9. A.J. Biacchi, D.D. Vaughn II, R.E. Schaak, J. Am. Chem. Soc., 2013, **135**, 11634−11644.
10. Y.J. Zhang, J. Lu, S.L. Shen, H.R. Xu, Q.B. Wang, Chem. Commun., 2011, **47**, 5226-5228.
11. J.-G. Kang, J.-G. Park, D.-W. Kim, Electrochem. Commun., 2010, **12**, 307–310.
12. J. Lu, C.Y. Nan, L.H. Li, Q. Peng, Y.D. Li, Nano Research, 2013, **6(1)**, 55-64.
13. H.B. Wu, A.Q. Pan, H.H. Hang, X.W. Lou, Adv. Funct. Mater., 2013, **23**, 5669-5674.
14. J.H. Pan, Q.Z. Huang, Z.Y. Koh, D. Neo, X.Z. Wang, Q. Wang, ACS Appl. Mater. Interfaces, 2013, **5(13)**, 6292-6299.
15. J.S. Chen, Y.N. Liang, Y.M. Li, Q.Y. Yan, X. Hu, *ACS Appl. Mater. Interfaces*, 2013, **5 (20)**, 9998-10003.
16. H.K. Wang, K.P. Dou, W.Y. Teoh, Y.W. Zhan, T.F. Hung, F.H. Zhang, J.Q. Xu, R.Q. Zhang, A.L. Rogach, *Adv. Funct. Mater.*, 2013, **23**, 4847-4853.
17. L. Shi, H.L. Lin, *Langmuir*, 2010, **26(24)**,18718-18722.
18. S.K. Li, Z.G. Wu, W.H. Li, Y. Liu, R.F. Zhuo, D. Yan, J. Wang, P.X.Yan, *CrystEngComm*, 2013, **15**, 1571-1577
19. Q. An, Q. Wei, L. Mai, J. Fei, X. Xu, Y. Zhao, M. Yan, P. Zhang, S. Huang, *Phys. Chem. Chem. Phys.*, 2013, **15**, 16828-16833.
20. S.J. Ding, D.Y. Zhang, H.B. Wu, Z.C. Zhang, X.W. Lou, *Nanoscale*, 2012, **4**, 3651-3654.
21. M.S. Park, Y.M. Kang, G.X. Wang, S.X. Dou, H.K. Liu, Adv. Funct. Mater., 2008, 18, 455–461.
22. D.D. Vaughn II, O.D. Hentz, S. Chen,D. Wang, R.E. Schaak, Chem. Commun., 2012, **48**, 5608-5610.
23. C. Wang, G.H. Du, K. Ståhl, H.X. Huang, Y.J. Zhong, J.Z. Jiang, J. Phys. Chem. C, 2012, 116, 4000-4011.
24. S.J. Ding, X.W. Lou, Nanoscale, 2011, 3, 3586-3588.
25. C.Y. Cao, W. Guo, Z.M. Cui, W.G. Song, W. Cai, J. Mater. Chem., 2011, 21, 3204-3209.
26. C.X. Zhai, N. Du, H. Zhang, D.R. Yang, Chem. Commun., 2011, 47, 1270-1272.
27. G.G. Kumar, K. Reddy, K.S. Nahm, N. Angulakshmi, A.M. Stephan, J. Phys. Chem. Solids, 2012, 73, 1187-1190.
28. J. Xia, G.C. Li, Y.C. Mao, Y.Y. Li, P.K. Shen, L.P. Chen, CrystEngComm, 2012, 14, 4279-4283.

29. H.K. Wang, L.J. Xi, J. Tucek, Y.W. Zhan, T.F. Hung, S.V. Kershaw, R. Zboril, C.Y. Chung, A.L. Rogach, Nanoscale, 2013, 5, 9101-9109.
30. Y. Lee, S.R. Bae, B.J. Park, D.W. Shin, W.J. Chung, Y.M. Kang, J. Am. Ceram. Soc., 2012, 95(7), 2272-2276.
31. J. Xia, G.C. Li, Y.C. Mao, Y.Y. Li, P.K. Shen, L.P. Chen, CrystEngComm, 2012, 14, 4279-4283.
32. H.K. Wang, L.J. Xi, J. Tucek, Y.W. Zhan, T.F. Hung, S.V. Kershaw, R. Zboril, C.Y. Chung, A.L. Rogach, Nanoscale, 2013, 5, 9101-9109.
33. Y. Lee, S.R. Bae, B.J. Park, D.W. Shin, W.J. Chung, Y.M. Kang, J. Am. Ceram. Soc., 2012, 95(7), 2272-2276.
34. J. Wang, Y.C. Liu, S.Y. Wang, X.T. Guo, Y.P. Liu, J. Mater. Chem. A, 2014, 2, 1224-1229.